JOM, Vol. 72, No. 4, 2020
https://doi.org/10.1007/s11837-019-04001-w

Three-Dimensional Laser Engraving for Fabrication of Tough Glass-Based Bioinspired Materials

AHMED S. DALAQ[1] and FRANCOIS BARTHELAT[1,2,3]

1.—Department of Mechanical Engineering, McGill University, 817 Sherbrooke Street West, Montreal, QC H3A 2K6, Canada. 2.—Department of Mechanical Engineering, University of Colorado, 427 UCB, 1111 Engineering Dr, Boulder, CO 80309, USA. 3.—e-mail: francois.barthelat@colorado.edu

Glass has many attractive properties including transparency, durability, low electrical conductivity, and corrosion resistance, but its brittleness still limits the range of its applications. Three-dimensional laser engraving has been explored to generate three-dimensional (3D) networks of weak interfaces within the bulk of glass. These interfaces deflect cracks and dissipate energy by friction, with mechanisms that are similar to fracture in mollusk shells or teeth. Confocal microscopy was used to characterize the morphology of laser-induced microcracks in borosilicate glass and ceramic glass, and the effective toughness of laser-engraved interfaces was measured. The effect of microcrack spacing on interface morphology, damage parameter, fracture surface, and fracture toughness was explored. Architectured borosilicate glass panels based on a simple grid pattern were then fabricated. These all-brittle panels do not require mechanical confinement and can absorb significantly more impact energy than monolithic glass provided that the interface toughness is tuned properly.

INTRODUCTION

Glass is a relatively hard and stiff material with excellent optical properties, low thermal expansion, low electrical conductivity, chemical resistance, corrosion resistance, and durability.[1–3] These properties make glass attractive for manufacturing mirrors, glass wares, windows, windshields, or glass facades. However, the strength of glass is very sensitive to defects, and fracture in glass is brittle and catastrophic. Several methods have been developed to improve the mechanical properties of glass. Thermal or chemical tempering can increase the strength of glass, but not its toughness.[1,4] Laminating glass can improve its damage tolerance, but its impact resistance and toughness are not improved significantly.[5] The inherent brittleness of glass can be addressed by incorporating microarchitectures within the bulk, using heterogeneities compositions, weak interfaces, and controlled geometrical features.[6–8] For example, adding ductile particles to glass can hinder crack growth by pinning and crack bridging,[9,10] improving the toughness by 60 times. However, residual stresses and debonding between the metal and glass phases limit the efficacy of this method. Recently, other approaches based on manipulating larger-scale features have emerged, and such architectured materials are a powerful approach to produce multifunctional materials that combine tunable strength, toughness, and some attractive thermal and electrical properties.[6,11–13] Architectured materials may come in different arrangements such as sandwiched, lattices, and segmented forms. Sandwiched structures are well suited for lightweight flexural applications (plates and beams), while lattices are effective for shock absorption.[14,15] Segmented materials are another type of architectured materials which can confine damage, deflect cracks, and increase toughness.[8,16,17] Interestingly these toughening strategies are also found in hard biological materials such as bone, teeth, and mollusk shells.[11,12,18,19] These materials are segmented into smaller building blocks made of hard minerals, bonded by softer, organic-rich interfaces. For example, in mollusk shell nacre, the minerals come in the form of microscopic tablets bonded with soft organic layers to form a three-dimensional brick wall (Fig. 1a). The interplay between the architecture and the interface properties generates powerful inelastic

(Published online January 27, 2020)

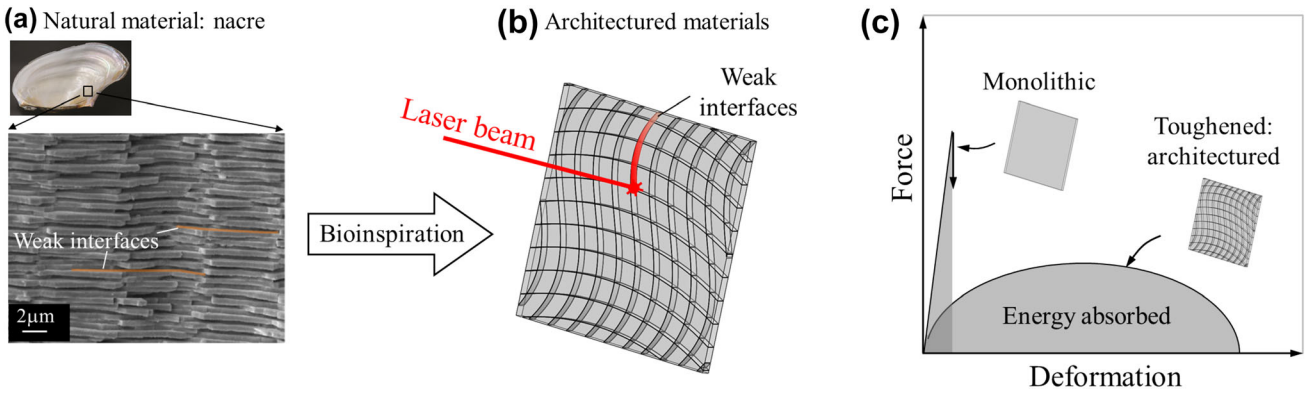

Fig. 1. (a) Nacre is a hard biological material where the interplay between microarchitecture and weak interfaces generates unique mechanisms and high toughness (adapted from Refs. 35 and 22); (b) these concepts are inspiring new architectured materials; (c) Ideal force–deformation curves for monolithic and architectured material.

mechanisms that make nacre three orders of magnitude tougher than its brittle constituents.[20–22] Nacre has therefore served as a model and inspiration for the design of tougher materials built from brittle components (ceramics, glasses) (Fig. 1-b).[20,23–26] Many other materials in Nature display such segmentation, including fish fins,[27,28] spines[12,29] and tesserae in shark skeletons.[19] These periodic arrangements of hard structural elements are reminiscent of masonry, where building blocks with well-defined geometries are assembled to form self-standing lintels, domes, overhanding components, or interlocked pavements. Masonry structures have indeed recently inspired topologically interlocked materials (TIMs),[30–33] a class of materials made of separated blocks that can interact by sliding and interlocking upon loading, resulting in tougher materials. The shape of the blocks and the properties (friction, adhesion, and energy dissipation) of the interfaces can be tuned to achieve different combinations of stiffness, strength, and toughness.[12,16,34] In particular, architecture can be used to generate nonlinear and large deformation at the interfaces, turning brittle monolithic materials into deformable structures (Fig. 1c).

The concepts of bioinspiration, microarchitecture, and topological interlocking have recently been implemented in transparent glass. In particular, we recently demonstrated that three-dimensional (3D) laser engraving can be used to make glass-based TIM panels,[36] cross-ply glasses,[37] and nacre-like glasses.[25] These architectured glasses showed unusual deformation mechanisms and very high toughness and impact resistance with the addition of polymeric transparent layers. Three-dimensional laser engraving is a promising method to "carve" microarchitectures within glass,[38] but the micro- and mesostructures of the laser-engraved interfaces are not well understood. In addition, most recent architectured materials have either used completely separated blocks (e.g., TIMs[36]), or utilized the toughening mechanisms of ductile constituents, as in the addition of polymers in nacre-like glass.[25,37] Here we mainly consider the toughness of engraved interfaces in glass and their toughening effects without including ductile materials, so the analysis is based on all-brittle materials. In this report, we characterize the microscopic and mesoscopic structure of interfaces carved within the bulk of borosilicate glass and ceramic glass. We then expand on existing glass-based engraved material and present new designs which are based on all-brittle materials, which can operate in free-standing conditions (i.e. without the need for external mechanical confinement by a frame or ligaments).

LASER-ENGRAVED INTERFACES: FABRICATION AND 3D MORPHOLOGY

A fundamental element of architectured glass is the creation of weaker interfaces which can deflect and channel propagating cracks. Here we use a three-dimensional laser engraver (Vitrolux; Vitro Laser Solutions UG, Minden, Germany) to carve these weak interfaces. The engraver uses a nanosecond laser that emits a 355-nm ultraviolet (UV) pulse at frequency of 4 ns to 5 ns (0.5 W continuous wave pumped, 4 kHz repetition rate), which is focused at specific points within the bulk of glass. Nanosecond lasers generally form a plasma within nanoseconds at the focal point. This plasma quickly decays by releasing thermal energy into the material,[39–43] causing a rapid and localized increase in local temperature. The resulting high thermal stresses create microcracks within the volume of glass, at discrete points within the volume of glass where the laser beam is focused. We chose to engrave on borosilicate and ceramic glass, because they have low density, low thermal expansion, and low refractive index.[1] There applications are diverse, ranging from cookware, electronics, laboratory glass ware, dental cartridges, telescopes, glass facades, to radar

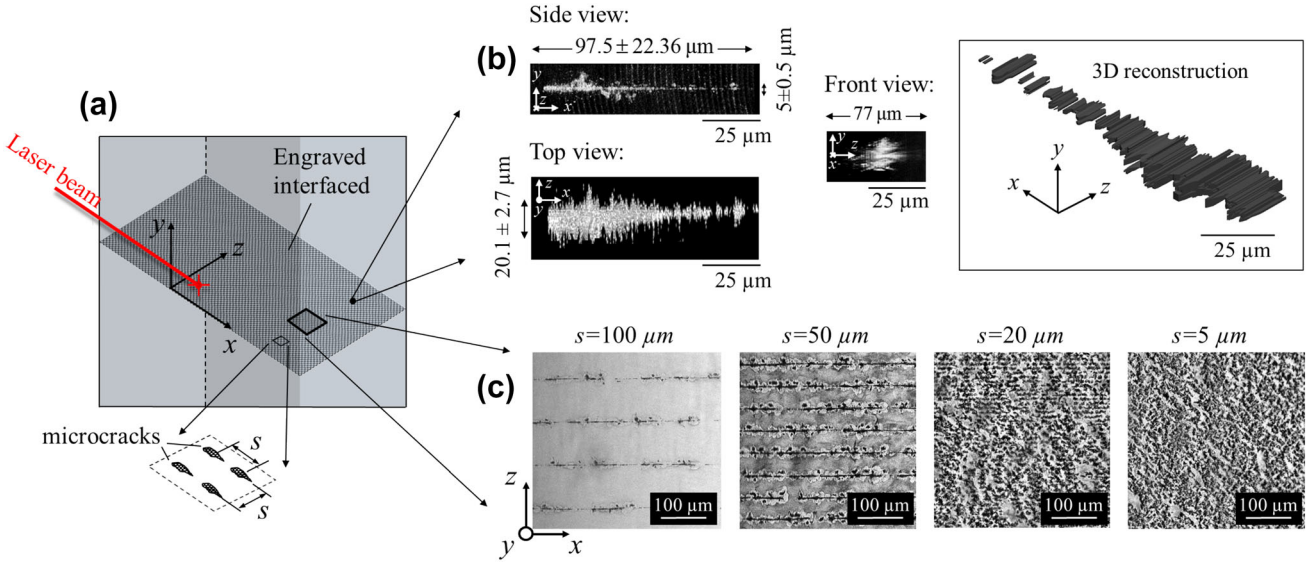

Fig. 2. (a) Schematic of engraved interface showing orientations, laser beam direction, and microcrack spacing; (b) Confocal microscope images of individual microcrack generated in borosilicate with a focused laser pulse; (c) Confocal images of engraved interface showing the microcrack distribution for s = 100 μm, 50 μm, 20 μm, and 5 μm.

protection units of aircraft nosecones.[44,45] Figure 2a shows a planar interface in the x–z plane that contains a square array of laser-engraved microcracks with spacing s, engraved with a laser beam parallel to the x-axis. In all of the experiments in this report, we engraved interfaces with different microcrack spacings s = 100 μm, 50 μm, 20 μm, 5 μm, 2 μm, and 1 μm using fixed laser power of 400 mJ, which was adequate to generate microcracks in the materials considered here. Increasing the laser power increases the size of the microcracks, as reported in Ref. 46. The size of the defects is also governed by the coefficient of thermal expansion (CTE) of the material, since most of the microdamage is generated by localized thermal stresses.[38]

An optical confocal microscope (Leica SP8, Germany) was used to characterize the three-dimensional morphology of individual microcracks in the material. Figure 2b shows front, side, and top views of a typical microcrack in borosilicate glass, together with its 3D reconstruction. The largest dimension of the microcrack is about 100 μm, being aligned with the x-direction (the direction of the incident laser beam), which may be due to spherical aberration in the laser focusing lens and/or Rayleigh scattering[47] (Fig. 2b). The microcrack is narrower along the other two directions, being about 5 μm and 20 μm along the y- and z-direction, respectively. Because of the local microdamage induced by the nanosecond laser, the outline of the microcracks is rough and irregular. It is also useful to assess how microcracks interact within the engraved interfaces. Figure 2c shows arrays of microcracks with spacings of s = 100 μm, 50 μm, 20 μm, and 5 μm. The size of the microcrack along the x-direction is larger than the spacing between the microcracks, thus they coalesced along this direction. The confocal images indeed show that the coalescence of the microcracks formed parallel lines along the x direction for s = 100 μm and 50 μm. For s = 20 μm, the spacing was small enough for the microcracks to also coalesce along the z-direction. For s = 5 μm, all the microcracks coalesced, so that the damaged areas were more diffused and randomly distributed.

AN IMAGE-BASED DAMAGE PARAMETER

The confocal images (Fig. 2c) were used to assess the degree of damage at the interfaces for different microcrack spacings s. The raw confocal images were converted into binary (black and white) images using an image thresholding method. All images were first subjected to a bandpass Fourier-transform filter to remove small features and speckles. The images were then converted to binary using the Phansalkar local thresholding method[48] (Supplementary Materials S1). This thresholding method is robust and produced clear and consistent outlines of microcracks, especially for images containing particle-like features. In the resulting images, black areas indicate fractured regions of the interface, while white areas indicate intact connected glass (ligaments, Fig. 3a). A damage parameter was then computed from these images as

$$\phi = \frac{A_c}{A} = 1 - \frac{A_l}{A}, \tag{1}$$

where A is the total area of image, A_c is the total black area representing the cracked portion of the interfaces, and A_l is the total area of the white portion representing the ligaments. Higher values

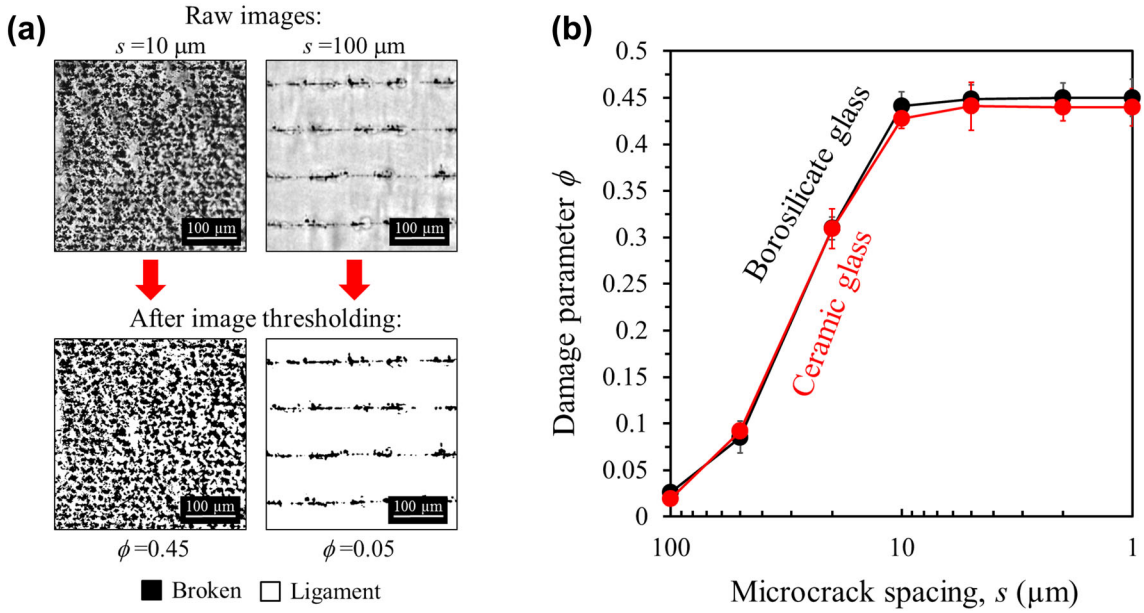

Fig. 3. (a) Two examples of raw images from confocal microscopy converted to binary images using a thresholding technique; (b) The binary images were used to estimate a damage parameter ϕ, plotted here as a function of the microcrack spacing s.

of ϕ therefore indicate higher levels of interface damage and weaker interfaces. Figure 3b shows how the damage parameter ϕ evolved when s was decreased for both types of glass. Large spacing (100 μm) barely damaged the interface, with $\phi \sim 0.025$. The microcrack spacing had the most effect on the damage in the range of 10–50 μm, in which the damage rapidly increased to $\phi \sim 0.45$. The effect of the microcrack spacing seemed to saturate for $s \leq 5$ μm. Interestingly, the response of ceramic glass and borosilicate glass to laser exposure was nearly identical.

FRACTURE TOUGHNESS AND FRACTOGRAPHY OF ENGRAVED INTERFACES

To measure the toughness of the engraved interfaces as a function of the microcrack spacing and glass type, single-edge notch bending (SENB) samples were prepared with length of 250 mm, width of 5 mm, and thickness of 3.2 mm. A notch with depth of 0.6 mm was created using a precision diamond saw (Struers, OH) (Supplementary Fig. S2), and the samples were then laser engraved to generate the weak interfaces. Using laser engraving to carve the entire length of the notch was possible but required high power and special microscopic examinations to ensure that the material was fully cut. Fracture tests were then conducted by loading the sample in a three-point bending configuration, following the testing standard in Ref. 49 (Fig. S2a, b). The fracture toughness of bulk glass $K_{IC}^{(b)}$ was measured as a reference ($K_{IC}^{(b)} = 1.032 \pm 0.18$ MPa$\sqrt{\text{m}}$ for borosilicate glass and $K_{IC}^{(b)} = 1.056 \pm 0.04$ MPa$\sqrt{\text{m}}$ for ceramic glass), and the toughness of the interfaces $K_{IC}^{(i)}$ created with different microcrack spacings. Figure 4a shows the experimental fracture toughness of engraved planes normalized by the fracture toughness of bulk glass $K_{IC}^{(i)}/K_{IC}^{(b)}$ for different microcrack spacings s and for borosilicate glass and ceramic glass. The fracture toughness of the interface was close to that of bulk glass for $s = 100$ μm but rapidly decreased when the microcrack spacing was decreased to $s = 10$ μm. Further decrease of the microcrack spacing ($s < 10$ μm) had a lesser effect on the toughness. We were not able to "cut" the sample at the laser engraving stage. Although microcracks coalesced for $s = 5$ μm, 2 μm, and 1 μm, the ligaments that bear loads evidently persisted, preventing complete separation of the interface during laser engraving. There was a slight increase in the fracture toughness at $s = 1$ μm, possibly because of geometrical interlocking at the heavily damaged interfaces.

Figure 4b shows optical microscopy images of the fractured surfaces for samples created with six different microcrack spacing. The fracture surfaces exposed the microcracks induced by the laser, particularly the lines parallel to x-axis seen under the confocal microscope. The spacing of these lines matched the microcrack spacing s set at the laser engraving stage, confirming that these lines were induced by the laser rather than resulting from crack propagation due to external loading. However, these engraved lines could only be seen for $s = 100$ μm and $s = 50$ μm. For $s = 10$ μm, such lines were not visible, and the fracture surface had

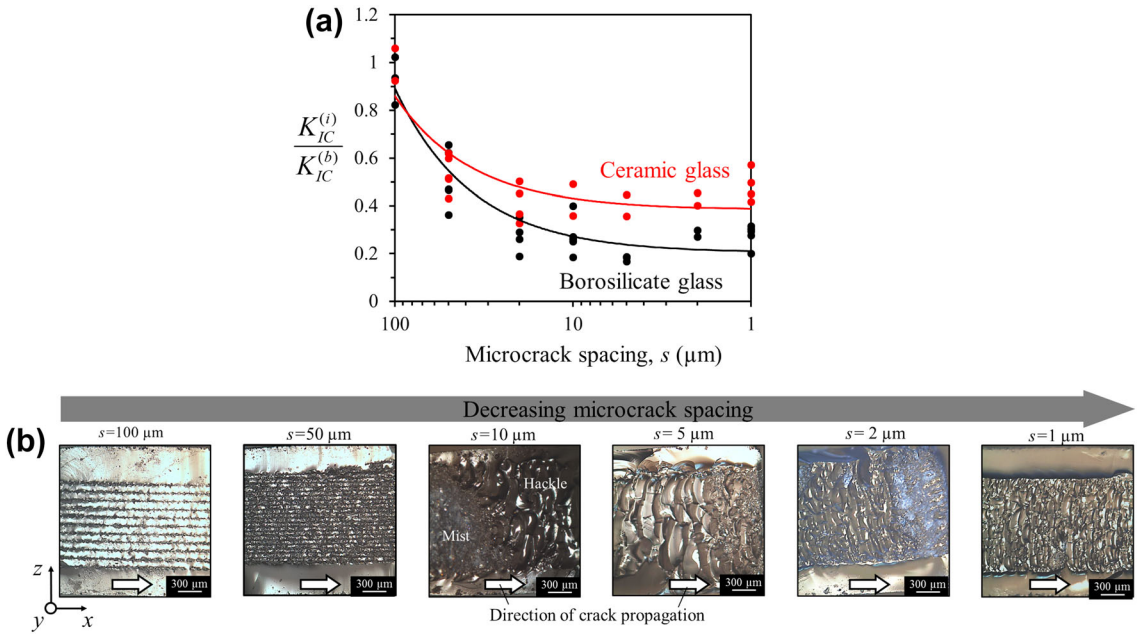

Fig. 4. Experimental results of fracture tests: (a) Relative fracture toughness $K_{IC}^{(i)}/K_{IC}^{(b)}$ plotted as a function of the microcrack spacing for ceramic glass (red) and borosilicate glass (black); (b) Optical images of fracture surfaces for different microcrack spacings s. The macrocrack induced by the external load propagated from left to right along the x-direction (Color figure online).

a more typical mist-and-hackle appearance. The texture of the fracture surface became rougher along the x-direction, forming a "hackle region" which indicates that the macrocrack induced by external loading propagated out of the x–z plane.[50] Interestingly, the texture became denser and more detailed for $s < 5$ μm, which typically indicates that the interface was under higher stresses.[50] This inference is consistent with the slight increase in fracture toughness measured for $s < 5$ μm.

PREDICTING THE FRACTURE TOUGHNESS OF ENGRAVED INTERFACES

Based on the results of the image analysis and fracture test presented above, there was evidently a strong correlation between the initial damage induced by the laser and the apparent fracture toughness of the interface. Experiments clearly showed an exponential or power-law decay of $K_{IC}^{(i)}/K_{IC}^{(b)}$ with more damage. Knowing the size and spacing of the microcrack, it is in theory possible to predict the apparent toughness of the interfaces. The simplest fracture model gives a trend $K_{IC}^{(i)}/K_{IC}^{(b)} \propto \phi/\tan(\phi)$,[51] confirming that the apparent toughness will decrease with damage. Other analytical[52,53] and numerical[54] fracture models follow a similar trend, but with additional factors that account for the shape and distribution of microcracks. However, none of these fracture-mechanics-based models can predict the decrease of toughness observed experimentally in this work for smaller microcrack spacings. A likely explanation for this discrepancy is the lack of order and periodicity in the microcracks and their tendency to coalesce during engraving, especially for $s < 50$ μm (Fig. 2c). Alternatively, a simple micromechanics model based on a porous plane could capture this randomness at engraved planes.[55–57] The model assumes open porosity at the interface and a linear elastic response which is in direct correlation with the areal fraction of solid ligaments. This assumption translates into a phenomenological relationship with Young's modulus of $E^* = E(1-\phi)^p$,[56] where E and E^* are the Young's modulus of nonengraved and engraved samples, respectively. This model also translates into a reduction of the surface fracture energy $\gamma^* = \gamma(1-\phi)^q$.[56] One may therefore write[56,57]

$$\frac{K_{IC}^{(i)}}{K_{IC}^{(b)}} = (1-\phi)^n, \tag{2}$$

where γ and γ^* are the surface energy of nonengraved and engraved samples, respectively. The powers p, q, and n are empirical constants.

Equation 2 is plotted for the experimental data for different ϕ values in Fig. 5a and b, where the least-squares method is used to minimize the residuals and find the exponents n that fit the experiments. For borosilicate, the exponent is n = 3.98 with R^2 = 0.88. For ceramic glass the exponent is n = 1.98, which is lower than that of borosilicate. This indicates that the borosilicate glass incurred more damage than the ceramic glass. As a result, borosilicate glass exhibited a sharper decay in toughness with increased ϕ compared with the ceramic glass, possibly because the latter exhibits

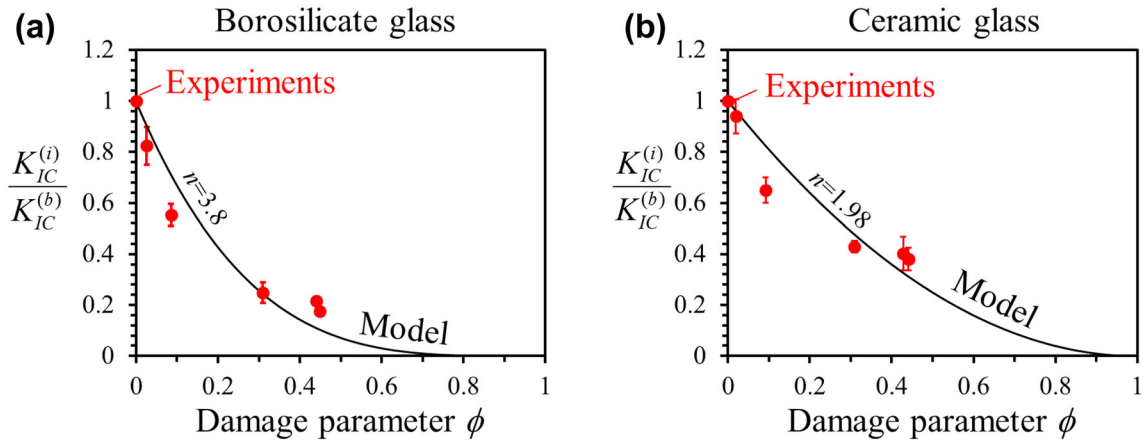

Fig. 5. Capturing the experimental model using an empirical model for (a) borosilicate glass and (b) ceramic glass.

almost zero thermal expansion[2] while the former has a slight coefficient of thermal expansion ($\sim 3 \times 10^{-6}$ 1/K at room temperature[1]). The thermal stresses in the borosilicate glass were therefore higher during laser engraving, resulting in more damage. The exponent n can capture the two different behaviors of materials based on the different materials interaction with the laser, which depend for example on the thermal expansion, transparency, and composition of the glass. The model in Eq. 2 is based on area fractions, and the measured area fractions remained unchanged for $s < 5$ μm (Fig. 3b). This model is thus unable to capture the slight increase in toughness for $s < 5$ μm.

EXAMPLE: LASER-ENGRAVED ARCHITECTURED PANELS

Using a well-calibrated laser engraving protocol, interfaces with specific fracture toughness can be created within the bulk of glass. In this example, we fabricated architectured glass panels whose mechanical properties are governed by weaker interfaces and microarchitectures, in ways similar to mollusk shells, teeth, or bone.[11] Borosilicate glass panels (50 mm × 50 mm × 3 mm) served as base materials for these experiments. Samples with these dimensions are easy to handle during engraving and experiments, and they are relevant for many glass applications. We engraved the glass panels through their full thickness following a grid pattern that partitioned the panel into 7 × 7 blocks, where each block was 6.25 mm × 6.25 mm × 3 mm in size (Fig. 6a). The microcrack spacing for laser engraving was adjusted to generate weak interfaces with different relative toughness $K_{IC}^{(i)}/K_{IC}^{(b)}$. Unlike traditional, topologically interlocked panels formed of completely separated blocks,[16,33] the blocks in the engraved architectured panels shown in Fig. 6b are still attached by weak interfaces ($K_{IC}^{(i)} > 0$). Therefore, the engraved glass panels do not require assembly, can be easily handled, and do not require special supports, abutments, or mechanical confinement by external frames or ligaments.

We tested the architectured glass panels under impact loading using an instrumented impact tower (Instron CEAST, MA, US) in the setup shown in Fig. 7a. The architectured panel was simply supported on a steel frame and was struck by a steel impactor with a semispherical tip (r = 2.4 mm) at a speed of 2.2 m/s. The kinetic energy of the crosshead and impactor (about 1.2 J) was large enough that no significant decrease in speed was recorded when the impactor fractured the sample. The force history was recorded using a 3-kN piezoelectric load cell embedded near the tip of the impactor. The impact lasted on average for 3 ms, thus the stages of deformation before, at, and after impact could be captured by taking snapshots at a rate of 1000 frames/second using a high-speed camera.

Figure 7b shows the impact force F as a function of the displacement u for the monolithic glass panels $K_{IC}^{(i)}/K_{IC}^{(b)} = 1$ (indicated in black) and for architectured glass panels with different levels of interface toughness $K_{IC}^{(i)}/K_{IC}^{(b)}$ = 0, 0.19, 0.24, 0.34, and 0.55 (indicated in red). For the monolithic sample, the impact force F rose quickly until a maximum of about 2000 N, after which *it* dropped suddenly at u = 0.3 mm, corresponding to the complete fracture of the panel. Small fluctuations in the force were attributed to elastic waves and vibrations. Figure 7c shows high-speed snapshots captured during the impact. For the monolithic sample, the impactor tip impacted the panel at the center, where high local contact stresses generated multiple radial cracks from the point of impact. The panel fractured catastrophically and into many fragments (Supplementary Video S1). In contrast, architectured panels showed a quick increase in force up to 600 N and a slow progressive decrease in F until complete fracture at around u = 2.9 mm, which is almost ten

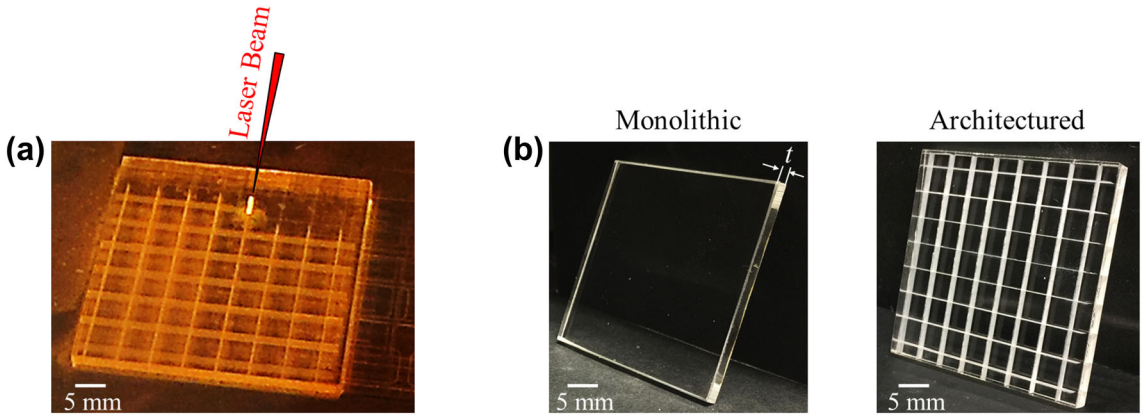

Fig. 6. (a) Laser engraving a 7 × 7 grid pattern through the thickness of a monolithic glass panel to create an architectured glass panel; (b) borosilicate glass panel before engraving (monolithic) and after engraving (architectured).

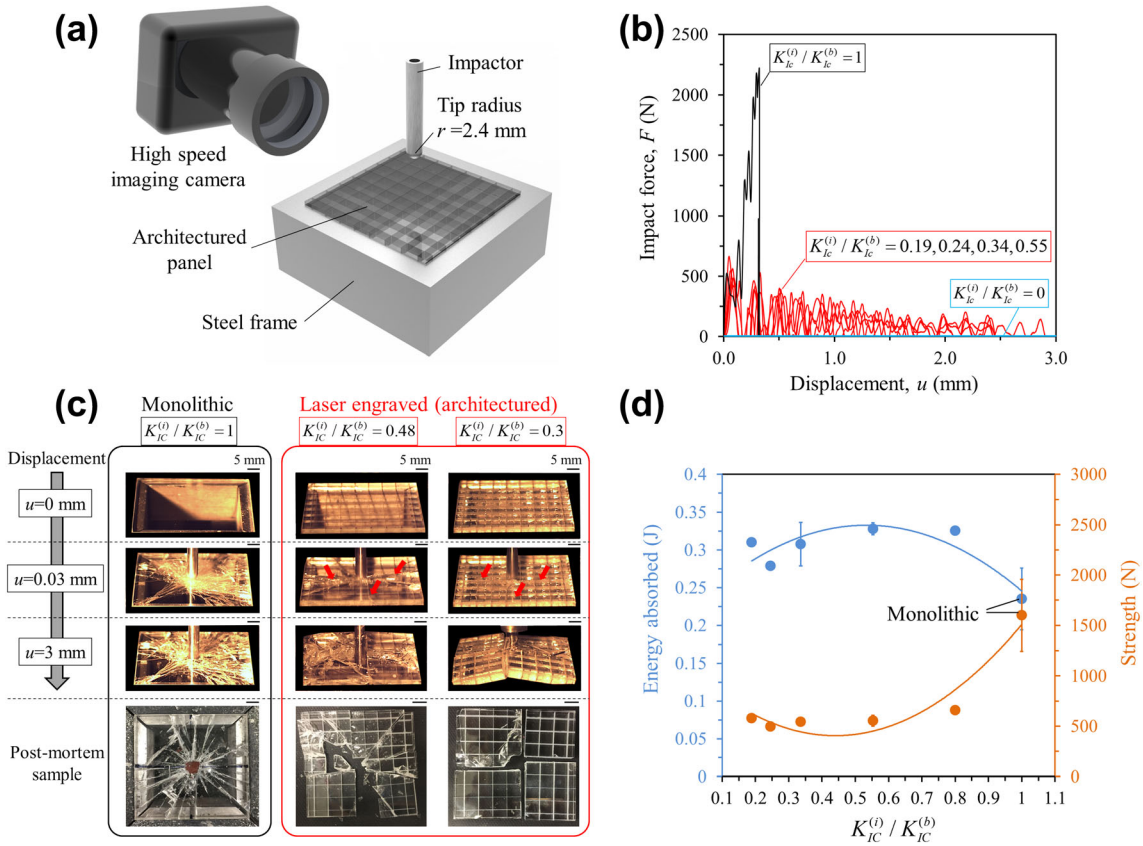

Fig. 7. (a) Experimental setup for impact testing of borosilicate glass panels and high-speed imaging; (b) impact force–displacement curve for monolithic and architectured panels; (c) corresponding high-speed images and post mortem pictures; the red arrows indicate crack deflection and pinning (d) energy absorbed (in dark blue) and strength (in orange) of architectured panels fabricated with different interface fracture toughness values (Color figure online).

times the maximum displacement for the monolithic panel. Cracks propagated mostly along the weak interfaces of the grid pattern (marked by red arrows in Fig. 7c). For $K_{IC}^{(i)}/K_{IC}^{(b)} = 0.48$, some cracks were deflected along the interfaces while others were pinned by the grid (post mortem images in Fig. 7c). The number of fragments was also much smaller than for the monolithic glass. Interestingly, for weaker interfaces with $K_{IC}^{(i)}/K_{IC}^{(b)} = 0.3$, almost all cracks propagated along interfaces and the panel fractured into four clean parts (Supplementary Video S2). Unlike the monolithic panel, these panels

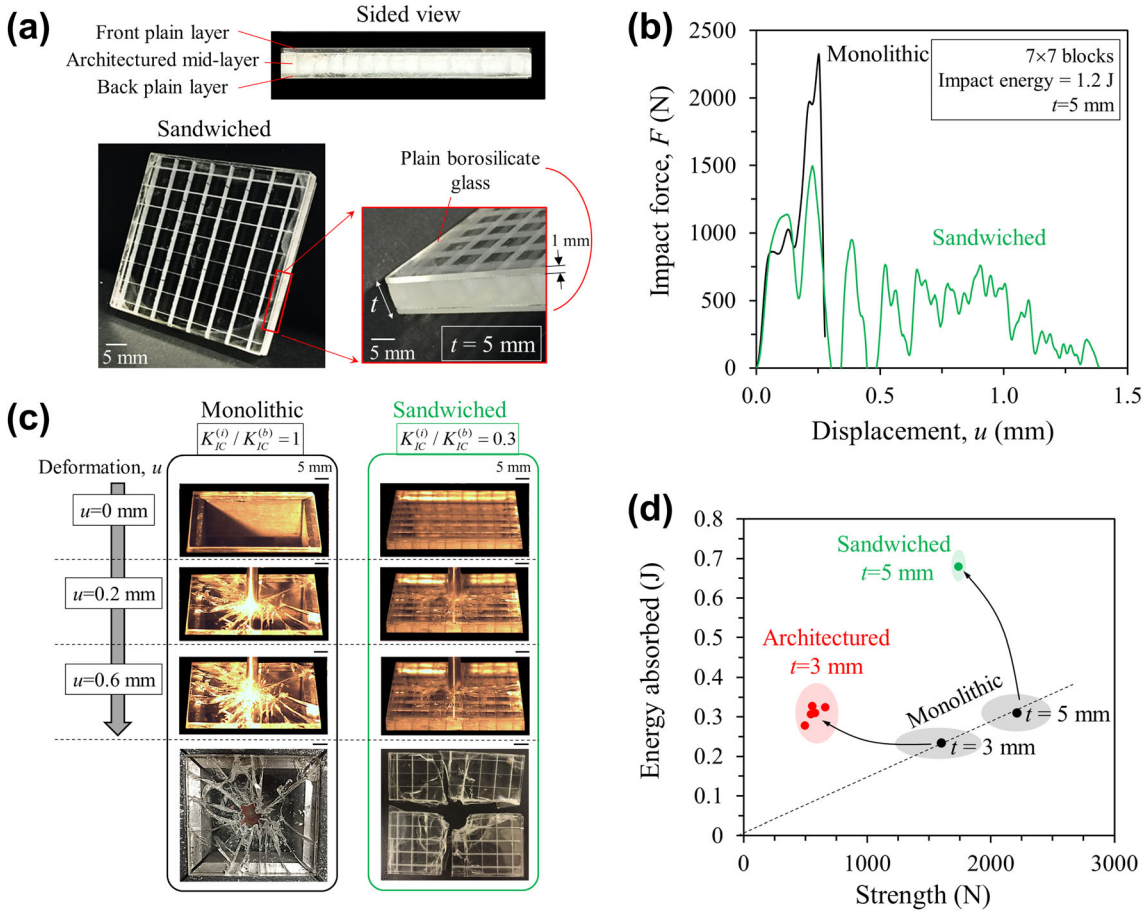

Fig. 8. (a) Schematic and pictures of the sandwiched architecture glass panel; (b) $F - u$ curves for monolithic panel and sandwiched panels; (c) high-speed snapshots during impact at u = 0 mm, 0.2 mm, and 0.6 mm, with post mortem images; (d) summary of all tests results on an Ashby-like plot of strength versus energy absorbed.

could be reassembled and reused for another cycle of loads, either by regluing the parts or by using stiff confining frames as in conventional TIMs made from separate blocks. The larger displacements sustained by the architectured glass panel can be explained by the weak interfaces, which once broken can interact by jamming, sliding, and hinging.[12]

From the impact force–displacement ($F - u$) curves, the strength (maximum force) and the energy absorption of the panel were determined by calculating the total area under the curves (Fig. 7d). Architectured panels with $0.189 < K_{IC}^{(i)}/K_{IC}^{(b)} < 1$ absorbed up to 75% more energy (an additional 0.13 J) than the monolithic panel ($K_{IC}^{(i)}/K_{IC}^{(b)} = 1$). The additional 0.13 J is dissipated by the breaking of interfaces, sliding of blocks, and crack deflection and pinning. These mechanisms are possible because the interfaces are weaker than the bulk material, although on the other hand very weak interfaces are detrimental because interfacial fracture would be too easy. The experimental measurements shown in Fig. 7d reveal that the energy absorption was highest for an optimum interface fracture toughness of $K_{IC}^{(i)}/K_{IC}^{(b)} = 0.328$. However, this improvement in the toughness for the architectured panels came at the expense of strength, which was 60% lower for the architectured compared with the monolithic glass panels. To address this drawback, we considered designs where a layer of architectured borosilicate glass (with $K_{IC}^{(i)}/K_{IC}^{(b)} = 0.3$) was sandwiched between two 1-mm-thick monolithic borosilicate panels. The two panels were glued to the front and back side of the architectured layer using cyanoacrylate adhesive (Fig. 8a). We performed impact tests on the resulting materials using the same protocol as described above. However, in this case, the total thickness of the sandwiched material was 5 mm, thus for comparison we also tested 5-mm-thick plain borosilicate panels. Figure 8b shows representative $F - u$ curves for monolithic (in black) and sandwiched architectured panels (in green). As expected, the failure of the monolithic panel was brittle and catastrophic, with a peak force of about 2250 N. Interestingly the architectured panel was almost as strong, with a peak force of about 1500 N, but the

deformation of the sandwiched architectured panel was more progressive and graceful than in the monolithic case (Supplementary Video S3). Figure 8c shows high-speed snapshots taken at different stages of deformation for the 5-mm-thick monolithic panel and the sandwiched architectured panels. The monolithic panel showed the same brittle and catastrophic failure as the 3-mm-thick plain samples described above. For the sandwiched architectured panel, the snapshots showed that the initial peak of force was generated by the front plain panel, and the fracture of the front layer resulted in the first drop of force observed in the F–u curve. The remainder of the curve corresponds to the progressive failure of the architectured midlayer, which involves blocks interacting by sliding and hinging. It is not clear from these data and imaging at which point the plain back layer fractures, but at about u = 1.5 mm the panel has completely failed. The failure mode of the sandwich material is still governed by the architecture of the midlayer, with the panels fracturing into clean parts (post mortem images in Fig. 8c).

Figure 8d shows an Ashby chart of strength versus energy absorption for all the samples tested in this work. The monolithic panels were relatively strong, but with little energy absorption. Thicker panels were stronger and absorbed more energy, these two properties scaling linearly with the thickness of the panel (dashed line). Thicker samples were also more prone to failure by sliding (shearing of the interfaces) due to their lower span-to-thickness ratio, whereas thinner samples were prone to failure by interface opening (hinging).[12] The 3-mm-thick architectured panels absorbed 40% more energy than the 3-mm-thick monolithic panel, but at the expense of a 60% drop in strength. The sandwiched architectured panels absorbed 2.2 times more energy than the 5-mm-thick monolithic panel, for a loss of strength of only 27%. These results suggest that the front and back plain layers in the sandwich design not only increase strength but also enhance energy dissipative mechanisms in the architectured midlayer, probably by confining the architectured blocks and increasing frictional dissipation.

Single-phase architectured materials as used in this work rely on geometry and the presence of interfaces for toughening (e.g., sliding and crack pinning) or strengthening mechanisms (e.g., jamming of blocks). In multiphase architectured materials, additional characteristic such as damping effects can be added to the materials by the addition of viscoelastic phases. The addition of soft materials to interfaces can reduce contact stresses, control friction, vary the failure mode, and provide an additional energy dissipation mechanism. However, the absence of any polymer in single-phase architectured materials is advantageous for high-temperature applications. More complex patterns (with $K_{IC}^{(i)} > 0$), such as hexagonal or circular patterns, may generate additional in-plane confinement that results in more jamming between blocks and therefore greater strength overall.

CONCLUSIONS

The morphology of individual microcracks generated by discrete laser pulses focused within glass was characterized, as well as the effects of the microcrack spacing on the morphology of the engraved interfaces within the bulk of glass. Confocal imaging and a local thresholding method were used to compute a damage parameter ϕ which can be used to predict the fracture toughness of interfaces based on a simple model. A simple square pattern was then engraved into glass panels, and the toughness of the interfaces was manipulated to generate different combinations of strength and toughness. The following conclusions can be drawn from the results of this study:

1. In these experiments, the power of the laser was maintained at a constant value (400 mW). At this power, confocal images revealed that individual microcracks have dimensions of about 100 μm, 20 μm, and 5 μm, and that they are elongated along the laser beam direction.
2. For microcrack spacings $s > 100$ μm, discrete microcracks were observed at the interfaces. For $s \leq 100$ μm, coalescence of microcracks was observed along the direction of laser engraving. For $s \leq 20$ μm, coalescence of microcracks was observed along all directions. The effect of decreasing the microcrack spacing on the damage parameter saturated for $s \leq 10$ μm.
3. Decreasing the microcrack spacing rapidly decreased the interface toughness from $K_{IC}^{(i)}/K_{IC}^{(b)} = 1$ down to $K_{IC}^{(i)}/K_{IC}^{(b)} = 0.38$, over the range of 10 μm $\leq s \leq$ 100 μm. The weakening effect saturated at s = 10 μm. Reducing the microcrack spacing to smaller values $s <$ 10 μm had little additional effect on the fracture toughness. However, even at the smallest microcrack spacing (s = 1 μm), the interface was never entirely cut because some ligaments persisted across the interface.
4. The damage parameter ϕ could be used to predict the fracture toughness of the interfaces using a simple empirical model.
5. Engraved glass panels designed and fabricated in this way are made from all-brittle components and can operate in free-standing condition. Compared with plain glass, more progressive and graceful force–displacement curves were observed under impact loads, with the maximum deformation being almost 10 times and the energy absorption 75% higher. In basic designs, this improvement in toughness was at the expense of a 60% loss in strength.
6. In contrast to monolithic glass panels, where

failure was catastrophic, the architectured glass panels broke into four parts along the engraved interface. Unlike monolithic panels, the broken parts of architectured panels could be reassembled and reused with the aid of side supports, ligaments, or glue.

7. To address the 60% loss in strength of the simply engraved design, the engraved layer was sandwiched between two thin monolithic panels, which reduced the loss in strength from 60% to 27%. In addition, this design improved the toughness, probably because of the additional confinement of the architectured blocks.

The results of this study show how 3D laser engraving can be used in glass to generate weak interfaces without completely cutting the material into blocks. The interfaces are strong enough that the engraved glass panels can be handled without separation of the blocks but weak enough to deflect cracks and prevent them from spreading and growing across blocks, even in the absence of mechanical confinement. This fabrication method may be applicable to other transparent materials such as acrylic, poly(methyl methacrylate) (PMMA), and other types of glass. The laser engraving method is amenable to the design and fabrication of many microarchitecture designs, many of which could be inspired from architectures found in hard biological materials.

ACKNOWLEDGEMENTS

We thank Prof. Allen J. Ehrlicher (bioengineering department, McGill) for providing access and training for the confocal microscope facility at his laboratory. This work was supported by a Strategic Grant (STPGP 479137-5) from the Natural Sciences and Engineering Research Council of Canada and by a Team Grant (191270) from the Fonds de Recherche du Québec – Nature et Technologies. A.D. was partially supported by a McGill Engineering Doctoral Award.

ELECTRONIC SUPPLEMENTARY MATERIAL

The online version of this article (https://doi.org/10.1007/s11837-019-04001-w) contains supplementary material, which is available to authorized users.

REFERENCES

1. J.E. Shelby and M. Lopes, *Introduction to Glass Science and Technology*, 2nd ed. (Cambridge: Royal Society of Chemistry, 2005).
2. A.K. Varshneya, *Fundamentals of Inorganic Glasses* (New York: Gulf Professional, 1994).
3. L. Wondraczek, J.C. Mauro, J. Eckert, U. Kühn, J. Horbach, J. Deubener, and T. Rouxel, *Adv. Mater.* 23, 4578 (2011).
4. F. Petit, A.C. Sartieaux, M. Gonon, and F. Cambier, *Acta Mater.* 55, 2765 (2007).
5. H.S. Norville, W. King Kim, and L. Swofford Jason, *J. Eng. Mech.* 124, 46 (1998).
6. M.F. Ashby, *Philos. Mag.* 85, 3235 (2005).
7. M.F. Ashby, *Materials Selection in Mechanical Design*, 5th ed. (Cambridge, MA: Butterworth-Heinemann, 2016).
8. O. Bouaziz, Y. Bréchet, and J.D. Embury, *Adv. Eng. Mater.* 10, 24 (2008).
9. V.V. Krstic, P.S. Nicholson, and R.G. Hoagland, *J. Am. Ceram. Soc.* 64, 499 (1981).
10. H. Huang, H. Ke, P. Zhang, Z. Pu, D. Zou, P. Zhang, T. Shi, L. Zhang, and T. Liu, *Mater. Des.* 157, 371 (2018).
11. F. Barthelat, *Int. Mater. Rev.* 60, 413 (2015).
12. A.S. Dalaq and F. Barthelat, *Int. J. Solids Struct.* 171, 146 (2019).
13. D.W. Abueidda, A.S. Dalaq, R.K. Abu Al-Rub, and I. Jasiuk, *Compos. Struct.* 133, 85 (2015).
14. A.S. Dalaq, D.W. Abueidda, and R.K. Abu Al-Rub, *Compos. Part A Appl. Sci. Manuf.* 84, 266 (2016).
15. J. Song, W. Zhou, Y. Wang, R. Fan, Y. Wang, J. Chen, Y. Lu, and L. Li, *Mater. Des.* 173, 107773 (2019).
16. M. Mirkhalaf, T. Zhou, and F. Barthelat, *PNAS* 115, 9128 (2018).
17. H. Yazdani Sarvestani, M. Mirkhalaf, A.H. Akbarzadeh, D. Backman, M. Genest, and B. Ashrafi, *Mater. Des.* 167, 107627 (2019).
18. F. Barthelat, *Philos. Trans. R. Soc. A Math. Phys. Eng. Sci.* 365, 2907 (2007).
19. P. Fratzl, O. Kolednik, F.D. Fischer, and M.N. Dean, *Chem. Soc. Rev.* 45, 252 (2016).
20. N. Abid, M. Mirkhalaf, and F. Barthelat, *J. Mech. Phys. Solids* 112, 385 (2018).
21. R.Z. Wang, Z. Suo, A.G. Evans, N. Yao, and I.A. Aksay, *J. Mater. Res.* 16, 2485 (2001).
22. F. Barthelat, H. Tang, P.D. Zavattieri, C.M. Li, and H.D. Espinosa, *J. Mech. Phys. Solids* 55, 306 (2007).
23. N. Abid, J.W. Pro, and F. Barthelat, *J. Mech. Phys. Solids* 124, 350 (2019).
24. H. Zhu, H. Cao, X. Liu, M. Wang, X. Meng, Q. Zhou, and L. Xu, *Mater. Des.* 175, 107783 (2019).
25. Z. Yin, F. Hannard, and F. Barthelat, *Science* 364, 1260 (2019).
26. T. Magrini, F. Bouville, A. Lauria, H.L. Ferrand, T.P. Niebel, and A.R. Studart, *Nat. Commun.* 10, 2794 (2019).
27. B.E. Flammang, S. Alben, P.G.A. Madden, and G.V. Lauder, *J. Morph.* 274, 1044 (2013).
28. M.E. Porter, R.H. Ewoldt, and J.H. Long, *J. Exp. Biol.* 219, 2908 (2016).
29. E.L. Troxell, *GSA Bull.* 36, 605 (1925).
30. A.V. Dyskin, Y. Estrin, A.J. Kanel-Belov, and E. Pasternak, *Adv. Eng. Mater.* 3, 885 (2001).
31. A.V. Dyskin, Y. Estrin, A.J. Kanel-Belov, and E. Pasternak, *Philos. Mag. Lett.* 83, 197 (2003).
32. Y. Feng, T. Siegmund, E. Habtour, and J. Riddick, *Int. J. Impact Eng.* 75, 140 (2015).
33. T. Siegmund, F. Barthelat, R. Cipra, E. Habtour, and J. Riddick, *Appl. Mech. Rev.* 68, 040803 (2016).
34. M. Mirkhalaf, A. Sunesara, B. Ashrafi, and F. Barthelat, *Int. J. Solids Struct.* 158, 52 (2019).
35. M.G. August. Pearl coating built from the ground up (*Chemistry World*, 2019), https://www.chemistryworld.com/news/pearl-coating-built-from-the-ground-up/1017294.article.
36. M. Mirkhalaf, J. Tanguay, and F. Barthelat, *Extreme Mech. Lett.* 7, 104 (2016).
37. Z. Yin, A. Dastjerdi, and F. Barthelat, *Acta Biomater.* 75, 439 (2018).
38. V. Rastogi, S. Chaurasia, and D.S. Munda, *J. Non-Crystall. Solids* 463, 138 (2017).
39. X. Zeng, X.L. Mao, R. Greif, and R.E. Russo, *Appl. Phys. A* 80, 237 (2005).

40. B.T. Do, M. Kimmel, M. Pack, R. Schmitt, and A.V. Smith, SPIE Proc. Conf. Laser-Induced Damage in Optical Materials, 853008 (2012).
41. K. Sugioka and Y. Cheng, *Light Sci. Appl.* 3, e149 (2014).
42. B. Wu and Y.C. Shin, *J. Appl. Phys.* 99, 084310 (2006).
43. V. Rastogi, S. Chaurasia, and D.S. Munda, arXiv:1601.03146 *[physics]*, (2016).
44. W. Martienssen and H. Warlimont, *Springer Handbook of Condensed Matter and Materials Data* (New York: Springer, 2006).
45. B. Karmakar, *Functional Glasses and Glass-Ceramics: Processing, Properties and Applications* (Cambridge, MA: Butterworth-Heinemann, 2017).
46. M. Mirkhalaf, A.K. Dastjerdi, and F. Barthelat, *Nat. Commun.* 5, 3166 (2014).
47. W.M. Steen and J. Mazumder, *Basic Laser Optics* (London: Springer, 2010).
48. P. Neerad, M. Sumit, S. Ashish, and J. Madhuri, in *2011 International Conference on Communications and Signal Processing*, vol. 218 (2011).
49. ASTM International. *Test Method for Measurement of Fracture Toughness (ASTM e-1820)*. E-1820-01 ed. (USA: ASTM International, 2004).
50. G.D. Quinn, *Fractography of Ceramics and Glasses* (Gaithersburg, Md: National Institute of Standards and Technology, 2007).
51. T.L. Anderson and T.L. Anderson, *Fracture Mechanics: Fundamentals and Applications*, 3rd ed. (New York: CRC, 2005).
52. H. Lekesiz, N. Katsube, S.I. Rokhlin, and R.R. Seghi, *Int. J. Solids Struct.* 50, 186 (2013).
53. H. Tada, P.C. Paris, and G.R. Irwin, *The Stress Analysis of Cracks Handbook*. 3 ed. (Three Park Avenue New York, 2000).
54. C.Y. Dong and K.Y. Lee, *Int. J. Fract.* 133, 389 (2005).
55. H. Jelitto and G.A. Schneider, *Acta Mater.* 151, 443 (2018).
56. A.S. Wagh, J.P. Singh, and R.B. Poeppel, *J. Mater. Sci.* 28, 3589 (1993).
57. B.D. Flinn, R.K. Bordia, A. Zimmermann, and J. Rödel, *J. Eur. Ceram. Soc.* 20, 2561 (2000).